

Full length article

Operating conditions combination analysis method of optimal water management state for PEM fuel cell



Wenxin Wan^a, Yang Yang^{a,b}, Yang Li^c, Changjun Xie^{a,b,d,*}, Jie Song^e, Zhanfeng Deng^e, Jinting Tan^f, Ruiming Zhang^g

^a School of Automation, Wuhan University of Technology, Wuhan, 430070, China

^b Hubei Key Laboratory of Advanced Technology for Automotive Components, Wuhan University of Technology, Wuhan, 430070, China

^c Department of Electrical Engineering, Chalmers University of Technology, Gothenburg, 41258, Sweden

^d Modern Industry College of Artificial Intelligence and New Energy Vehicles, Wuhan University of Technology, Wuhan, 430070, China

^e Global Energy Interconnection Research Institute, Beijing, 102211, China

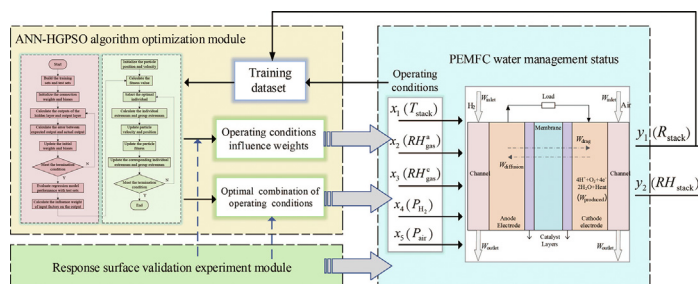
^f State Key Laboratory of Advanced Technology for Materials Synthesis and Processing, Wuhan University of Technology, Wuhan, 430070, China

^g Guangdong Hydrogen Energy Institute of Wuhan University of Technology, Foshan, 528000, China

HIGHLIGHTS

- Internal resistance-operating condition model to assess humidity state.
- Model trends of operating conditions on water management state.
- Impact weights of each operating condition on water management state.
- Optimal operating combination for the best water management state.
- Higher efficiency and accuracy compared to response surface methodology results.

GRAPHICAL ABSTRACT



ARTICLE INFO

Keywords:

PEMFC
Water management status
Internal resistance-operating condition model
Operating condition optimization
Response surface method

ABSTRACT

The water content of proton exchange membrane fuel cells (PEMFCs) affects the transport of reactants and the conductivity of the membrane. Effective water management measures can improve the performance and extend the lifespan of the fuel cell. The water management state of the stack is influenced by various external operating conditions, and optimizing the combination of these conditions can improve the water management state within the stack. Considering that the stack's internal resistance can reflect its water management state, this study first establishes an internal resistance-operating condition model that considers the coupling effect of temperature and humidity to determine the variation trend of total resistance and stack humidity with single-factor operating conditions. Subsequently, the water management state optimization method based on the ANN-HGPSO algorithm is proposed, which not only quantitatively evaluates the influence weights of different operating conditions on the stack's internal resistance but also efficiently and accurately obtains the optimal combination of five operating conditions: working temperature, anode gas pressure, cathode gas pressure, anode gas humidity, and cathode gas humidity to achieve the optimal water management state in the stack, within the entire range of current densities. Finally, the response surface experimental results of the stack also validate the effectiveness and accuracy of the ANN-HGPSO algorithm. The method mentioned in this article can provide effective strategies for efficient water management and output performance optimization control of PEMFC stacks.

* Corresponding author.

E-mail address: jackxie@whut.edu.cn (C. Xie).

| Nomenclature | | V_{stack} | Volume of the stack, cm^3 |
|----------------------------|---|--------------------|--|
| | | t | Exhaust emission time, s |
| | | Greek | |
| N | Number of single cells | α | Electrochemical reaction constant |
| R_{stack} | Total internal resistance, Ω | γ | Adjustment factor |
| R_f | Activation resistance, Ω | δ | Thickness of diffusion layer, μm |
| R_m | Ohmic resistance, Ω | η | Learning rate |
| R_d | Concentration loss resistance, Ω | σ | Convergence factor |
| R | ideal gas constant, $\text{J}/(\text{mol}\cdot\text{K})$ | λ | Membrane water content |
| F | Faraday constant | μ | Number of transferred electrons |
| i | Current density, A/cm^2 | τ | Number of moles of transferred ions |
| T_{stack} | Stack temperature, K | ω | Connection weight |
| RH_{stack} | Relative humidity of stack, % | β | Conductivity coefficient |
| W_{stack} | Stack water content | Subscript | |
| t_m | Thickness of proton exchange membrane, μm | a | Anode electrode |
| S | Electrochemical reaction area, cm^2 | c | Cathode electrode |
| C_g | Total concentration of reactants, mol/L | Superscript | |
| D_{eff} | Water transfer coefficient, $\text{J}/(\text{mol}\cdot\text{K})$ | i | Index of elementary unit, $i = 1, 2, \dots, n$ |
| W_{produce} | Amount of water produced by the reaction | j | Index of elementary unit, $j = 1, 2, \dots, n$ |
| $M_{\text{H}_2\text{O}}$ | Water vapor molar mass, g/mol | h | Index of elementary unit, $h = 1, 2, \dots, n$ |
| W_{inlet} | Intake water content | k | Index of elementary unit, $k = 1, 2, \dots, n$ |
| W_{outlet} | Exhaust water content | Abbreviations | |
| $m_{\text{H}_2,\text{in}}$ | Humidification hydrogen quality, g | PEMFC | Proton exchange membrane fuel cell |
| RH_{gas} | Gas relative humidity | ANN | Artificial neural network |
| p_{sat} | Saturated vapor pressure, atm | HGPSO | Particle swarm optimization with grey wolf optimization and reverse learning |
| M_{H_2} | Hydrogen molar mass, g/mol | CPSO | Chaos particle swarm optimization |
| P_{H_2} | Hydrogen inlet pressure, bar | PSOGA | Particle swarm genetic algorithm |
| $m_{\text{O}_2,\text{in}}$ | Humidification oxygen quality, g | | |
| M_{air} | Air molar mass, g/mol | | |
| V | Intake flow, L/min | | |
| V_m | P_{air} molar volume of gas in standard state, L/mol air inlet pressure, bar | | |

1. Introduction

The demand for clean and efficient energy is continuously growing in today's society. Proton exchange membrane fuel cell (PEMFC) transforms chemical energy into both electrical and thermal energy, and not only has general advantages such as cleanliness and high energy conversion efficiency, but also has characteristics such as working temperature close to room temperature, fast start-up time, and no electrolyte leakage or corrosion [1]. Based on these advantages, PEMFCs are considered as an ideal solution for future portable and mobile power sources [2]. However, PEMFC system is a nonlinear, multivariable, and strongly coupled complex system, and its output performance is affected by multiple factors, including different PEMFC system operating conditions [3]. Due to the sensitivity of PEMFC to changes in electrical current, changes in operating conditions may cause membrane dryness or water flooding states, seriously affecting the stability and output performance of PEMFC, and even shortening their remaining lifespan [4]. Excessive internal water content in the stack can hinder reactant transport, while membrane dryness can reduce the proton exchange membrane conductivity, and in severe cases, cause irreversible membrane damage [5]. Therefore, studying the impact of different operating conditions on PEMFC output performance and optimizing the combination of operating conditions to achieve the best water management state can provide a basis for formulating the best water management strategy, enhance the output performance and stability of fuel cells, and extend their lifespan [6].

To investigate how various operating conditions affect the performance of PEMFC and optimize the control strategy of operating conditions to achieve efficient water management, it is necessary to first

establish a model that accurately reflects the actual performance of PEMFC. The output characteristic models of PEMFC are mainly divided into mechanism models, empirical models, and semi-empirical models based on their establishment principles. Mechanism models are mainly based on the internal mass transfer, heat transfer, and electrochemical reaction processes of the fuel cell. Nalbant et al. [7] studied the effect of temperature, humidity, and membrane material changes on the output performance of PEMFC in high-temperature environments by establishing a one-dimensional steady-state model of anode mixed reaction gas. Jahnke et al. [8] investigated the degradation mechanism of stack output performance by establishing a coupled relationship model between stack temperature, water content, and pressure. Vivona et al. [9] established a 2D output characteristic model for PEMFC in high-temperature environments to study the effect of cathode reaction gas concentration and humidity on stack output performance. Kahveci et al. [10] developed a three-dimensional model to investigate the performance of PEMFC with curved flow channels and examined how operating pressure and temperature humidity affect the output performance. Multidimensional mechanism models can accurately reflect the internal reaction process of the stack, but the derivation process is cumbersome and some parameters are difficult to obtain directly. Empirical models are simple formulas obtained from experimental data that explore output characteristics rules while ignoring internal reaction mechanisms. Semi-empirical models are constructed by using empirical formulas to replace some of the complex reaction mechanisms in mechanism models, combining the advantages of mechanism models and empirical models, with high accuracy and reduced computational complexity. Giner-Sanz et al. [11] established a

semi-empirical equivalent model by studying the effect of stack temperature and humidity on membrane water activity, which can simulate stack output characteristics well. The output performance model described above mainly relies on external circuit data such as output voltage and current as reference indicators. However, these data primarily indicate the external output features of the fuel cell and cannot effectively characterize the internal water and thermal management status of the stack or the relationship between them. Different external operating conditions determine different water management states inside the stack. Working under normal conditions ensures the stack obtains good and stable output performance. However, working under abnormal conditions, such as membrane dryness or flooding, which affects the internal electrochemical reactions, will cause significant changes in the internal resistance. Therefore, selecting the internal resistance as the reference indicator for output performance can more intuitively reflect the internal water management status. Khan et al. [12] modeled the membrane water content and internal resistance of PEMFC system by combining the load current and temperature, and proposed an internal resistance model that can be used for output state control and fault diagnosis systems in PEMFC. Tiss et al. [13] developed a new nonlinear state space dynamic non-isothermal model based on the internal resistance and the mass and energy equations, to investigate how liquid water in the gas diffusion layer affects the dynamic characteristics of the battery. Niya et al. [14,15] analyzed and studied the impedance characteristics of ohmic losses in PEMFC under high-frequency conditions, and proposed an impedance model to describe the reaction process inside the stack. In Refs. [16,17], establishing a membrane electrode water transport model based on the internal resistance, and proposing a water balance control strategy for water flooding faults. The equivalent circuit models established in the above references using the internal resistance as the reference indicator all contain an important physical quantity of relative humidity. However, in the actual operation process of PEMFC stacks, the internal relative humidity of the stack is difficult to measure and control directly. Therefore, in this paper, by analyzing the water and thermal reaction mechanism inside the stack and the water transfer process, the corresponding external operating conditions are used to replace the difficult-to-measure relative humidity. Based on the coupling relationship between humidity and temperature, an internal resistance-operating condition model for PEMFC stacks is established to intuitively reflect the water management status inside the stack, and provide a model basis for directly adjusting the water content inside the stack by changing the external operating conditions.

Several studies have examined how individual operating conditions affect the internal water content of PEMFC based on established output characteristic models or equivalent circuit models, providing a basis for adjusting the PEMFC water management status by changing the operating conditions. Futter et al. [18] created a transient two-dimensional physical continuum framework model to evaluate the performance of polymer electrolyte membrane fuel cells and investigated the effect of different ion concentration gradients on the fuel cell water management status. Kim et al. [19] explored the correlation between the oxygen diffusion rate in the catalyst layer and the distribution of liquid water within the fuel cell. Salahuddin et al. [20] examined the impact of enhancing the surface hydrophobicity of the gas diffusion layer on the water management status and electrochemical performance of the cell. Hernandez et al. [21] evaluated the impact of current ripple generated by external electronic devices on the water management status and output performance of fuel cells. In Refs. [17,22], analyzing the water transfer process within the fuel cell, and constructing an equivalent model considering inlet relative humidity, temperature, and reactant pressure to investigate the impact of relative humidity on the performance of PEM fuel cells. In addition, since the PEMFC system involves multiple external operating conditions and the internal water-thermal states are coupled with each other, the water management status of PEMFC is influenced by a combination of various external operating conditions. Therefore, it is imperative to horizontally analyze the impact of various operating

conditions on water management status based on the established internal resistance-operating condition model, clarify the degree of influence of each operating condition, and provide optimal operating condition combinations, so as to achieve the goal of improving the output capability of PEMFC by working at an optimal water management status.

Orthogonal experiment and response surface methodology are common experimental design methods for studying multiple factors and levels [23]. In Refs. [24,25], the impacts of operating temperature, relative humidity, and anode inlet pressure on PEMFC capability were studied using orthogonal experimental design, and the optimal operating parameter levels were determined. Kanani et al. [26] designed experiments using response surface methodology to model and investigate the impacts of temperature, humidity, and anode/cathode inlet flow ratio on stack power, and optimized the output power parameters. Mocoteguy et al. [27] used orthogonal experimental design to study the effect of stack temperature and humidity and the hydrogen/oxygen stoichiometry ratio on water management, and demonstrated that the stoichiometry ratio has a compensating effect on stack temperature and humidity. Some researchers used multiple-factor and multiple-level experimental design to explore the impacts of operating temperature, inlet pressure, and inlet flow ratio on relative humidity and stack performance [28–30]. Although experimental design methods can obtain the optimal combination of multiple factors, the experimental process is cumbersome, leading to low efficiency in obtaining optimal results. Moreover, the process of changing operating conditions to achieve different water management states inevitably results in PEMFC stack damage, such as membrane drying or flooding, which limits the application of these methods. The use of artificial intelligence optimization algorithms based on experimental data and precise PEMFC equivalent models to replace orthogonal experimental design or response surface methodology is a promising solution to determine the impact weights of input elements and the optimal operating parameter combination to achieve the goal of optimizing output performance. Chen et al. [31] proposed a multi-input and multi-output fuzzy control method for PEMFC thermal management by selecting cathode temperature and relative humidity as control objectives and setting cooling water flow rate and inlet gas humidity as control variables. In Refs. [32,33], using the support vector machine (SVM) regression process based on the PEMFC model and parameterizing identification results to study the impact weights of elements such as temperature, anode–cathode inlet pressure, and membrane water content on the output capability of the fuel cell. Nanadegani et al. [34] constructed a PEMFC output voltage model about the anode–cathode gas coefficient, relative humidity, and load current using artificial neural network algorithm (ANN) and optimized the stack output performance based on the model. Laribi et al. [41] optimized the impedance model of PEMFC using ANN and applied the model to investigate the impact of inlet temperature and humidity on fuel cell water management state.

Combining the nonlinear fitting ability of neural networks and the global optimization ability of particle swarm optimization algorithm, it is possible to efficiently and accurately obtain the extreme values of the model within the specified range, as well as the optimal input combination corresponding to the extremum. In this paper, an internal resistance-operation conditions model of PEMFC stack is established, and the impact of various operating conditions is determined by fitting the model using the artificial neural network (ANN) algorithm. Then, the reverse learning particle swarm optimization algorithm with grey wolf optimization (HGPSO) is used to perform extremum optimization and obtain the corresponding optimal operation condition combination. The main contributions of this paper can be summarized as follows: (1) Establishing a quantified relationship between the internal relative humidity of PEMFC and the external operable conditions, and constructing an internal resistance-operational condition model based on the temperature-humidity coupling relationship; (2) Utilizing the internal resistance-operational condition model and the Artificial Neural Network- Reverse Learning Particle Swarm Optimization with Grey Wolf

Optimization (ANN-HGPSO) algorithm to determine the influence weights of different operational conditions, such as working temperature, cathode inlet pressure, anode inlet pressure, cathode inlet humidity, and anode inlet humidity on the water management status, and rapidly obtaining the precise optimal operational condition combination for the best water management state in a non-destructive manner; (3) Verifying and comparing the results of the influence weights of operational conditions and the optimal operational condition combination obtained by the ANN-HGPSO algorithm with those obtained by the Response surface methodology experiment, demonstrating the accuracy of the ANN-HGPSO optimization algorithm.

The remaining sections of this article are organized as follows: **Modeling** presents the establishment of the internal resistance-operation condition model. **Model verification and simulation analysis** describes the validation process of the model and the simulation analysis of each factor. **The ANN-HGPSO optimization algorithm** mainly introduces the principle and implementation process of the ANN-HGPSO optimization algorithm. **Results and discussion** provides the implementation results of the ANN-HGPSO algorithm and validates the feasibility and accuracy of the algorithm with response surface verification experiments. Finally, the last chapter concludes the entire paper.

2. Modeling

Various operating conditions, including the fuel cell temperature, exert a substantial impact on the water management condition of the fuel cell. Different water management states correspond to different total internal resistances of the PEMFC, which in turn affect the performance of the cell. In order to ensure that the fuel cell operates in the optimal water management state at all times, and to reduce the internal resistance and improve the power generation efficiency, it is essential to optimize and regulate the external operational parameters of the fuel cell. Establishing a precise correlation between the internal resistance and operating conditions of the fuel cell is critical to achieve optimal water management conditions in the fuel cell. This paper establishes an internal resistance-operating condition model that considers the coupling relationship between temperature and humidity, and quantitatively analyzes the relationship between external operating conditions and the water management state of the fuel cell.

2.1. Model of internal resistance characteristics

The Randles equivalent circuit model is used to reflect the internal resistance characteristics of the fuel cell stack [33], as shown in Fig. 1. The total internal resistance of the stack R_{stack} mainly consists of activation resistance R_f , ohmic resistance R_m , concentration difference resistance R_d , and double-layer capacitance C_{dl} . Therefore, the DC internal resistance of the PEMFC stack can be approximately expressed by the following formula:

$$R_{\text{stack}} = N \cdot (R_f + R_m + R_d) \quad (1)$$

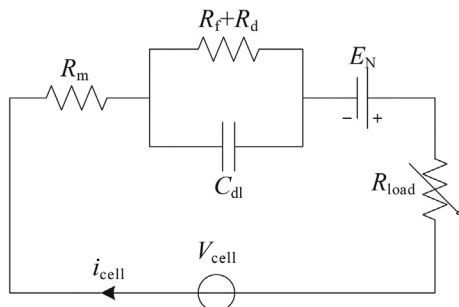


Fig. 1. Randles equivalent circuit model.

According to the electrochemical reaction kinetics, the hydrogen-oxygen reaction at the fuel cell electrode is a multi-step and multi-electron transfer reaction. In the initial stage of the reaction, it is necessary to overcome the activation energy barrier of the reactants to transform them from molecular to ionic states and release a large amount of energy. The charge transfer internal resistance R_f , which is the activation internal resistance, is the fundamental reason for the activation energy barrier. According to Tafel's equation, the activation internal resistance is related to the electrochemical reaction rate, temperature, current density, and other parameters [35]. The activation internal resistance can be approximated as:

$$R_f = \frac{R}{a\mu F i \times \exp[1,268(1/303 - 1/T_{\text{stack}})]} \quad (2)$$

The source of ohmic internal resistance R_m is the resistance of the cell materials to the movement of charges. In PEMFC, the equivalent impedance is mainly composed of the resistance experienced by the protonic positive charge passing through the exchange membrane, which is related to the thickness of the proton exchange membrane, the relative humidity and temperature inside the stack [36]. The numerical relationship can be expressed by the following formula:

$$R_m = \frac{t_m}{(0.513, 9\lambda - 0.326) \times \exp[1,268(1/303 - 1/T_{\text{stack}})]} \quad (3)$$

In order to maintain PEMFC in normal operating conditions, it is necessary to continuously deliver reactants and remove products from the fuel cell. In this process, concentration gradients are formed inside the components, which is the main reason for the occurrence of concentration loss internal resistance R_d . The concentration loss internal resistance is related to temperature, diffusion layer thickness, total concentration of reactants, etc [37], and can be represented by the following formula:

$$R_d = \frac{RT_{\text{stack}} \delta}{SC_g D_{\text{eff}} n^2 F^2} \quad (4)$$

As a supplement to these formulas:

$$n = [\beta \tau^2 F / RT]^{-1/2} \quad (5)$$

Furthermore, the water migration coefficient D_{eff} can be expressed as [36]:

$$D_{\text{eff}} = 10^{-6} \exp[2,416(1/303 - 1/T_{\text{stack}})] \cdot (2.563 - 0.33\lambda + 0.026, 4\lambda^2 - 0.000, 671\lambda^3) \quad (6)$$

The membrane water activity λ is related to the humidity RH_{stack} of fuel cell stack [38], and can be expressed by the following formula:

$$\lambda = 0.043 + 17.18RH_{\text{stack}} - 39.85RH_{\text{stack}}^2 + 36RH_{\text{stack}}^3 \quad (7)$$

The internal humidity parameter RH_{stack} in the above model equations is difficult to directly measure and temperature has a significant impact on humidity. Therefore, by considering the water transfer process inside the stack, a temperature and humidity coupling model is established to obtain the quantitative relationship between humidity and the changeable operating conditions outside. This allows for the development of an internal resistance-operating conditions model, which facilitates the exploration of the optimal operating combination under the best water management state in subsequent studies.

2.2. Internal resistance-operating condition model

The humidity RH_{stack} in the fuel cell is mainly determined by the amount of water in the stack. The change in the water content at time t inside the stack is related to the water content of the reactant gas entering the stack W_{inlet} , the water content of the exhaust gas leaving the stack

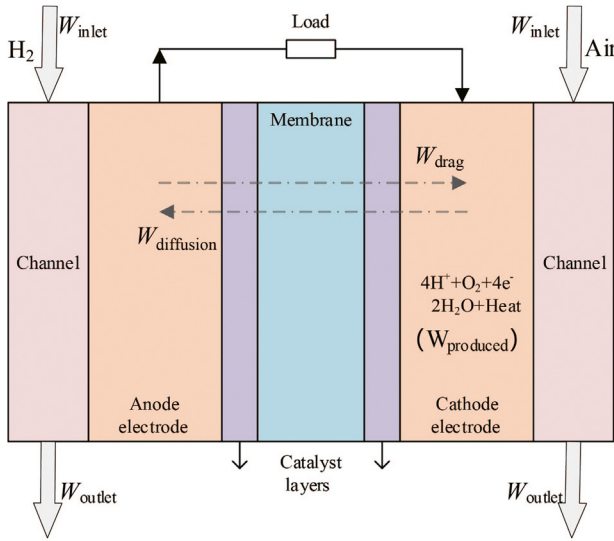


Fig. 2. Water transfer process inside the fuel cell.

W_{outlet} , the water produced by the reaction $W_{produced}$, and the water transferred inside the stack W_{drag} and $W_{diffusion}$, as shown in Fig. 2 [21].

Drawing from the assessment of the water transport mechanism in the fuel cell, it can be deduced that the moisture content within the stack remains in a relatively steady state. The total water content W_{stack} within the stack can be expressed as the following equation:

$$W_{stack} = W_{produced} + W_{inlet}^a + W_{inlet}^c - W_{outlet}^a - W_{outlet}^c \quad (8)$$

The amount of water generated by the reaction $W_{produced}$ can be expressed as [39]:

$$W_{produced} = M_{H_2O} \cdot NiS / 2F \quad (9)$$

The anode inlet water content W_{inlet}^a is related to the humidified hydrogen mass and the ratio of hydrogen humidity, and hydrogen gas and water vapor in the humidified hydrogen gas both satisfy the ideal gas equation [40]. Therefore, the anode inlet water content W_{inlet}^a can be expressed by the following formula:

$$W_{inlet}^a = \frac{m_{H_2, in} \cdot M_{H_2O} \cdot (RH_{gas}^a \cdot p_{sat})}{M_{H_2O} \cdot (RH_{gas}^a \cdot p_{sat}) + M_{H_2} \cdot (p_{H_2} - RH_{gas}^a \cdot p_{sat})} \quad (10)$$

The cathode inlet water content W_{inlet}^c is related to the mass and humidity ratio of the humidified air [40]. Thus, W_{inlet}^c can be represented by the following formula:

$$W_{inlet}^c = \frac{m_{O_2, in} \cdot M_{H_2O} \cdot (RH_{gas}^c \cdot p_{sat})}{M_{H_2O} \cdot (RH_{gas}^c \cdot p_{sat}) + M_{air} \cdot (p_{air} - RH_{gas}^c \cdot p_{sat})} \quad (11)$$

The total water content in the exhaust can be approximately represented by combining the absolute humidity with the ideal gas state equation. Water vapor mixed with a small amount of unreacted hydrogen is discharged as exhaust from the anode exhaust, while water vapor mixed with unreacted air is discharged from the cathode exhaust. Therefore, the total exhaust water content can be expressed as:

$$W_{outlet}^a + W_{outlet}^c = \left[\frac{M_{H_2O} \cdot p_{sat}}{RT_{stack}} \left(V_a - \frac{i \cdot V_m}{2F} \right) + \frac{M_{H_2O} \cdot p_{sat}}{RT_{stack}} \left(V_c - \frac{i \cdot V_m}{4F} \right) \right] \cdot t \quad (12)$$

Assuming that water inside the fuel cell exists in the gaseous state, the total water content W_{stack} in the stack is related to the fuel cell humidity RH_{stack} as follows [41]:

$$RH_{stack} = \frac{W_{stack} \cdot RT_{stack}}{M_{H_2O} \cdot p_{sat} \cdot V_{stack}} \quad (13)$$

As a supplement to the model formulas above, the saturation vapor pressure p_{sat} is only related to the operating temperature T_{stack} , and their quantitative relationship can be expressed as follows [35]:

$$\lg p_{sat} = -2.179 + 0.029, 5T_{stack} - 9.184 \times 10^{-5} T_{stack}^2 + 1.445 \times 10^{-7} T_{stack}^3 \quad (14)$$

Combining Eqs. (13) and (8) and taking into account the water content of each part, the relationship between the external operating conditions of PEMFC and the humidity RH_{stack} can be expressed by the following equation:

$$RH_{stack} = \left(\frac{NAi}{2F \cdot p_{sat}} + \frac{m_{H_2, in} \cdot RH_{gas}^a}{(M_{H_2O} - M_{H_2})RH_{gas}^a \cdot p_{sat} + M_{H_2} (p_{H_2} - RH_{gas}^a \cdot p_{sat})} \right) + \frac{m_{air, in} \cdot RH_{gas}^c}{(M_{H_2O} - M_{air})RH_{gas}^c \cdot p_{sat} + M_{air} (p_{air} - RH_{gas}^c \cdot p_{sat})} \cdot \left(\frac{4FR \cdot T_{stack}}{4F[V_{stack} + (V_a + V_c)t] - 3AV_m t \cdot i} \right) \quad (15)$$

By considering the influence of RH_{stack} as a parameter and substituting Eq. (15) into Eq. (7), the relationship between membrane water activity λ and external operating conditions can be expressed as follows:

$$\lambda = 0.043 + 17.18\xi_1(\xi_2 + \xi_3 + \xi_4) - 39.85\xi_1^2(\xi_2 + \xi_3 + \xi_4)^2 + 36\xi_1^3(\xi_2 + \xi_3 + \xi_4)^3$$

$$\begin{aligned} \xi_1 &= \frac{4FR \cdot T_{stack}}{4F[V_{stack} + (V_a + V_c)t] - 3AV_m t \cdot i} \\ \xi_2 &= \frac{NAi}{2F \cdot p_{sat}} \\ \xi_3 &= \frac{m_{H_2, in} \cdot RH_{gas}^a}{(M_{H_2O} - M_{H_2})RH_{gas}^a \cdot p_{sat} + M_{H_2} (p_{H_2} - RH_{gas}^a \cdot p_{sat})} \\ \xi_4 &= \frac{m_{air, in} \cdot RH_{gas}^c}{(M_{H_2O} - M_{air})RH_{gas}^c \cdot p_{sat} + M_{air} (p_{air} - RH_{gas}^c \cdot p_{sat})} \end{aligned} \quad (16)$$

Based on the coupling relationship between temperature and humidity, build the internal resistance-operation condition model. Integrating the previously established internal resistance model and the humidity-operation condition model, a resistance-operation condition model with the total internal resistance of fuel cell as the output and several operation conditions affecting the fuel cell output, such as battery temperature, cathode and anode inlet humidity, cathode and anode inlet pressure, as the input, is obtained.

3. Model verification and simulation analysis

3.1. Model verification

Based on the experimental data of PEMFC stack provided in references [21,42,43], the basic parameters of the stack and the ranges of various operating conditions are selected as shown in Table 1. Two sets of

Table 1
Range of fuel cell parameters and operating conditions.

| Stack parameters | Value | Stack parameters | Value |
|------------------------|---------------|------------------------------|---------|
| N | 12 | RH_{gas}^c (%) | 30–90 |
| S (cm ²) | 180 | p_{H_2} (bar) | 1–3 |
| t_m (μm) | 51 | p_{air} (bar) | 1.5–4.5 |
| T_{stack} (K) | 333.15–393.15 | V_a (L·min ⁻¹) | 30 |
| RH_{gas}^a (%) | 30–90 | V_c (L·min ⁻¹) | 75 |

experimental data corresponding to RH_{stack} and T of 50%/100% and 353.15K/393.15 K, respectively, are selected to verify the effect of stack humidity and temperature on the internal resistance. The relevant parameter S in the established internal resistance-operating condition model is changed to 4.4 cm^2 and the input data corresponding to the operating conditions are used. The model simulation process is completed through Simulink to obtain the R - I curve of each part of the simulated model and the comparison results with experimental data are shown in Fig. 3. From Fig. 3, it can be observed that the activation resistance rapidly decreases with increasing current density in a low current density environment, and then gradually stabilizes. The concentration loss resistance increases gradually with increasing current density, while the ohmic resistance is relatively stable at different current densities. Furthermore, alterations in humidity exert a greater influence on the internal resistance of the fuel cell than fluctuations in operating temperature. Simulation outcomes from the model align closely with empirical data, affirming the accuracy of the established model.

3.2. Simulation analysis

When the fuel cell temperature is 340 K, and the anode and cathode inlet pressures are 2 bar and 3 bar, respectively, and the inlet humidity to both anode and cathode is 60%, the curves of the fuel cell internal resistance R_{stack} and fuel cell humidity RH_{stack} versus current density are shown in Fig. 4(a). From Fig. 4(a), it can be observed that as the current density increases, the fuel cell internal resistance R_{stack} initially decreases rapidly, then tends to stabilize before gradually increasing, while the fuel cell humidity RH_{stack} monotonically increases. This is determined by the internal resistance characteristics of each component. At the low current density stage of the initial electrochemical reaction, the reactants undergo a transition from molecular to ionic state, driving the transfer of electrons, which must overcome activation energy barriers. At this stage, the total internal resistance is mainly determined by the magnitude of the activation internal resistance. In the subsequent medium current density stage, the ohmic resistance gradually tends to stabilize. At high current density stage, the electrochemical reaction intensifies, the amount of reactant gas increases, and the concentration gradient increases. At this point, the concentration loss internal resistance accounts for a relatively large proportion of the fuel cell total internal resistance. In response to this phenomenon, this article divides the current density into three regions: low, medium, and high, and selects representative current density values of 0.2 A/cm^2 , 0.5 A/cm^2 , and 1.0 A/cm^2 to evaluate the water management status based on the changes in R_{stack} . By optimizing the operable conditions and selecting the optimal combination of operating conditions at different current densities, R_{stack} is always kept to a minimum, thereby improving the power generation efficiency of PEMFC.

To investigate the impact of different operating conditions on the water management status of PEMFC, considering the difficulty of directly measuring and controlling the actual fuel cell humidity RH_{stack} , this study selects five factors: the operating temperature T_{stack} , the anode inlet pressure P_{H_2} , the cathode inlet pressure P_{air} , the anode inlet humidity RH_{gas}^a , and the cathode inlet humidity RH_{gas}^c for exploration. Firstly, the value of a single factor is changed within a certain range, and the change trend of the internal resistance R_{stack} with the corresponding operating condition is observed. Through the vertical analysis process of single factors, the approximate value range of each factor at the optimal water management state is determined. Fig. 4(b) to Fig. 4(f) represent the corresponding change trends of the fuel cell internal resistance when various operating conditions change under different current density environments.

1) The impact of temperature variation on the water management status is investigated in this part. Fig. 4(b) illustrates the fluctuations in stack resistance concerning the operating temperature range of 323.15–363.15 K. The anode and cathode inlet pressures are 2 bar and 3 bar, respectively, and both inlet humidities are 60%. The stack

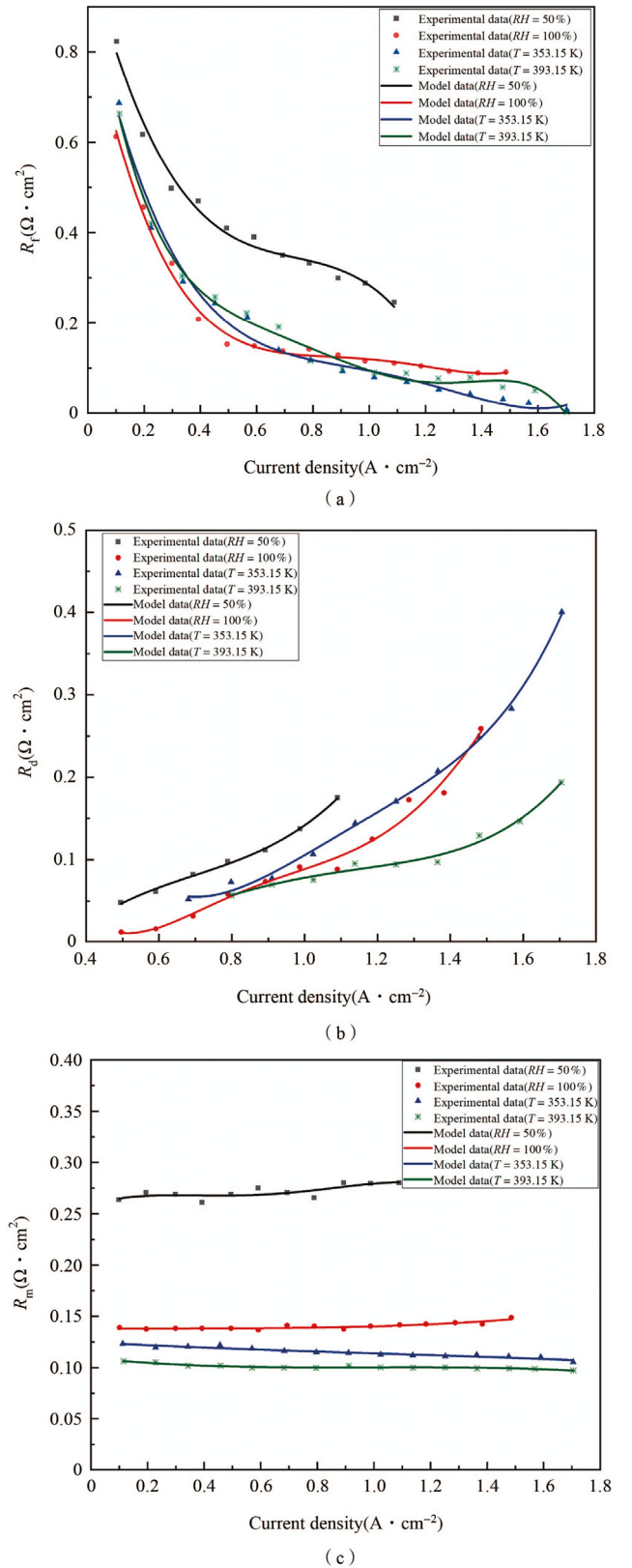


Fig. 3. The variation of internal resistance with current density. (a) Activation resistance. (b) Concentration loss resistance. (c) Ohmic resistance.

operates at low, medium, and high current densities. It can be observed that, at medium current density, the total resistance initially increases and then decreases with the increase of working temperature. Nevertheless, under low and high current density, the aggregate

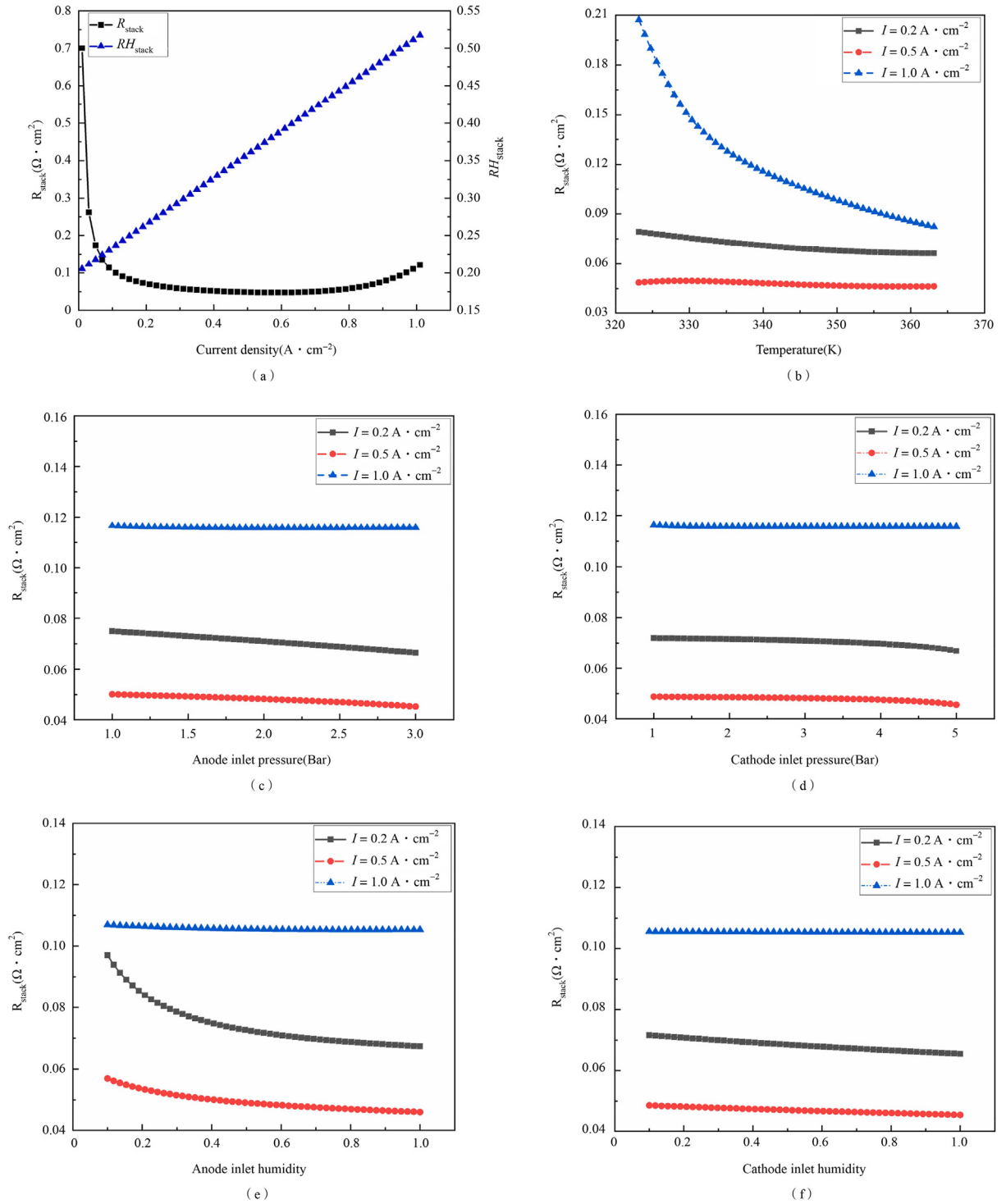


Fig. 4. Variation curves of internal resistance with different operating conditions. (a) Current density. (b) Operating temperature. (c) Anode inlet pressure. (d) Cathode inlet pressure. (e) Anode inlet humidity. (f) Cathode inlet humidity.

resistance decreases and eventually stabilizes as the operating temperature rises. Additionally, the decrease in total internal resistance is more pronounced in high current density conditions. This is because the increase in temperature enhances the activity of the catalyst, accelerates the electrochemical reactions and proton migration rate, and ultimately improves the output efficiency of the PEMFC;

2) The impact of changes in anode and cathode inlet pressure on the water management state is depicted in Fig. 4(c) and (d). At the

operating temperature of 340 K, the anode inlet pressure is varied between 1 bar and 3 bar while the cathode inlet pressure remains constant at 3 bar. Both anode and cathode inlet humidity are set at 60%. The system is subjected to operation at low, medium, and high current densities, and the resultant fluctuation in the internal resistance of the stack is graphically depicted. Fig. 4(d) depicts the change in the internal resistance of the stack with respect to the anode inlet pressure of 2 bar while the cathode inlet pressure is varied between 1

bar and 5 bar. It is observed that, for a constant current density, the internal resistance decreases gradually as the anode and cathode inlet pressure increases. This trend can be ascribed to the escalation in the effective partial pressure and gas solubility of hydrogen and oxygen, which stems from the amplified anode and cathode inlet pressure, correspondingly. This results in an acceleration of the diffusion rate of the reactant gases inside the stack, thus reducing the membrane transport resistance and enhancing the overall efficiency of the stack;

3) The impact of anode and cathode inlet humidity variations on water management is discussed. Fig. 4(e) depicts the fluctuations in the internal resistance of the stack under low, medium, and high current densities, with the anode and cathode inlet pressures being maintained at a constant level at 2 bar and 3 bar, respectively, and the anode inlet humidity ranges from 10% to 100% and the cathode inlet humidity is fixed at 60%, at the operating temperature of 340 K. Fig. 4(f) depicts the fluctuations in the internal resistance of the stack under low, medium, and high current densities, with the anode and cathode inlet pressures being maintained at a constant level at 2 bar and 3 bar, respectively, and the anode inlet humidity is fixed at 60% and the cathode inlet humidity ranges from 10% to 100%, at a operating temperature of 340 K. It is apparent that the internal resistance reduces and subsequently levels off with the increase in the anode and cathode inlet humidities, when current density is held constant. This is because the increase in anode and cathode inlet humidities leads to an increase in the membrane water content, which in turn enhances proton conductivity and improves the output efficiency of the stack.

Taking into account the operability range of the fuel cell and the rationality of model validation, the results of the single-factor simulation analysis and experimental data are considered, a range of values for each operating condition is selected for the subsequent exploration of the optimization method for the best water management state. Specifically, the selected ranges for operating conditions are: operating temperature of 330–350 K, anode inlet pressure of 1–3 bar, cathode inlet pressure of 1.5–4.5 bar, anode inlet humidity and cathode inlet humidity of 30%–90%.

4. The ANN-HGPSO optimization algorithm

The extremum-seeking optimization method of the artificial neural network (ANN) combined with the gray wolf optimization-based reverse learning particle swarm optimization (HGPSO) algorithm mainly consists of two parts: regression fitting of the ANN model and extremum seeking optimization of the particle swarm optimization (PSO) algorithm. Firstly, the internal resistance-operation condition model is used to obtain the dataset of internal resistance values and corresponding operating conditions. Then, the regression fitting process of the internal resistance prediction model is completed through the ANN module. The trained regression model is then used as the fitness function in the global optimization process of the HGPSO module, so as to efficiently and accurately obtain the output extremum of the internal resistance-operation condition model within the specified interval range, as well as the optimal input combination corresponding to the extremum.

4.1. ANN regression fitting module

The main structure of the neural network consists of three parts: the input layer I , the hidden layer H , and the output layer J , as shown in Fig. 5. The number of neurons i in the input layer corresponds to the number of inputs of the trained model, which in this paper correspond to the five selected operating conditions: operating temperature T_{stack} , anode inlet humidity RH_{gas}^a , cathode inlet humidity RH_{gas}^c , anode gas pressure P_{H_2} , and cathode gas pressure P_{air} . The number of neurons j in the output layer corresponds to the output of the model, which is the internal resistance R_{stack} of the fuel cell. The initial connection weights

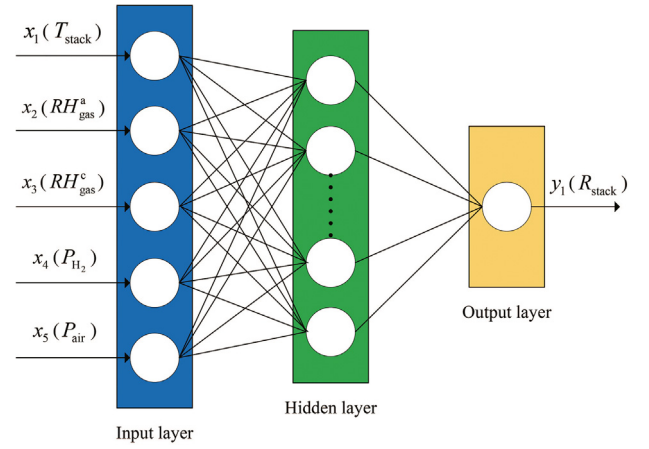


Fig. 5. Schematic diagram of the ANN structure.

between the input layer and hidden layer are denoted as ω_{ih} , the connection weights between the hidden layer and output layer are denoted as ω_{hj} , and the initial biases between the hidden layer and output layer are denoted as m_h and n_j . Therefore, the output of the input layer I of the network is:

$$y_i = x_i \quad (i = 1, 2, 3, 4, 5) \quad (17)$$

The activation function f in the network is chosen to be the commonly used sigmoid function, then the activation function are represented by:

$$f(x) = \frac{1}{1 + e^{-x}} \quad (18)$$

The output of the network's hidden layer H are represented by:

$$y_h = f\left(\sum_{i=1}^h \omega_{ih} y_i - m_h\right) \quad (19)$$

Similarly, the output of the network's output layer J are represented by:

$$y_j = f\left(\sum_{h=1}^j \omega_{hj} y_h - n_j\right) \quad (20)$$

The error can be given by the difference between the expected output y_0 and the actual output y_j , and the performance index function of the error function selected based on the gradient descent method can be expressed as:

$$E_{\text{Loss}} = \frac{1}{2} \sum_{j=1}^1 (y_0 - y_j)^2 \quad (21)$$

By applying backpropagation and iteratively adjusting the initial weights ω , biases m_h and n_j , and introducing the learning rate η to reduce the system error, the weights and biases are updated along the negative gradient direction. The amount of correction for each iteration Δy can be expressed as:

$$\Delta y = -\eta \cdot \frac{\partial E_{\text{Loss}}}{\partial y} \quad (22)$$

The updated expression for initial bias n_j of the output layer can be represented as:

$$n'_j = -\eta \cdot \frac{\partial E_{\text{Loss}}}{\partial y_j} \cdot \frac{\partial y_j}{\partial \left(\sum_{h=1}^j \omega_{hj} y_h - n_j\right)} \cdot \frac{\partial \left(\sum_{h=1}^j \omega_{hj} y_h - n_j\right)}{\partial n_j} + n_j \quad (23)$$

Similarly, the updated expression for connection weight ω_{hj} between the hidden layer and the output layer can be represented as:

$$\omega'_{hj} = -\eta \cdot \frac{\partial E_{\text{Loss}}}{\partial y_j} \cdot \frac{\partial y_j}{\partial \left(\sum_{j=1}^j \omega_{hj} y_h - n_j \right)} \cdot \frac{\partial \left(\sum_{j=1}^j \omega_{hj} y_h - n_j \right)}{\partial \omega_{hj}} + \omega_{hj} \quad (24)$$

The updated expression for initial bias m_h of the hidden layer can be represented as:

$$m'_h = -\eta \cdot \frac{\partial E_{\text{Loss}}}{\partial y_j} \cdot \frac{\partial y_j}{\partial \left(\sum_{j=1}^j \omega_{hj} y_h - n_j \right)} \cdot \frac{\partial \left(\sum_{j=1}^j \omega_{hj} y_h - n_j \right)}{\partial y_h} \cdot \frac{\partial y_h}{\partial m_h} + m_h \quad (25)$$

The updated expression for connection weight ω_{ih} between the input layer and the hidden layer can be represented as:

$$\omega'_{ih} = -\eta \cdot \frac{\partial E_{\text{Loss}}}{\partial y_j} \cdot \frac{\partial y_j}{\partial y_h} \cdot \frac{\partial y_h}{\partial \omega_{ih}} + \omega_{ih} \quad (26)$$

The model undergoes training and iterative adjustment by utilizing the data within the training set, aiming to achieve a level of output that satisfies the predefined error threshold. By calculating the corresponding layer-to-layer weights ω of the neurons for different input factors in the trained model, the weight of the impact of different input factors on the output results can be obtained. Finally, the regression performance of the neural network model is evaluated using test set data, and the model fitting effect can be quantified by metrics such as mean relative error (MRE), mean square error (MSE), root mean square error (RMSE), and squared correlation coefficient (R^2).

4.2. HGPSO extremum-seeking optimization module

The PSO algorithm achieves global optimization by iteratively adjusting the initial particles to approach the previously searched optimal solution in the swarm. However, traditional PSO algorithms suffer from slow convergence and the tendency to get trapped in local optima. To address these issues, the HGPSO algorithm used in this study incorporates opposition-based learning (OBL) and grey wolf optimization (GWO) on the basis of the PSO algorithm. This approach enhances the global search capability of the algorithm while optimizing the local search rate and accuracy near the optimal solution. As a result, the HGPSO algorithm is more efficient and accurate in completing the extreme optimization process.

The PSO algorithm consists of a population $\mathbf{X} = (X_1, X_2, \dots, X_q)$ composed of q particles, where vector X_k represents the position of the k -th particle in the search space D . By selecting the target function as the fitness function, the fitness value corresponding to each particle's position X_k can be calculated. The velocity of the k -th particle is denoted as $\mathbf{V}_k = [V_{k1}, V_{k2}, \dots, V_{kd}]^T$, and its personal best position is represented as $\mathbf{P}_k = [P_{k1}, P_{k2}, \dots, P_{kd}]^T$. The global best position of the population is $\mathbf{P}_g = [P_{g1}, P_{g2}, \dots, P_{gd}]^T$. During each iteration, the inertia weight ω_p , acceleration coefficients c_1 and c_2 , and two uniform random numbers r_1 and r_2 in the interval $[0,1]$ are introduced. s represents the current iteration number, and S_{\max} is the maximum number of iterations. The updating formulas for particle velocity V_{kd} and position X_{kd} can be expressed as:

$$V_{kd}^{s+1} = \omega_p V_{kd}^s + c_1 r_1 (P_{kd}^s - X_{kd}^s) + c_2 r_2 (P_{gd}^s - X_{kd}^s) \quad (27)$$

$$X_{kd}^{s+1} = X_{kd}^s + V_{kd}^{s+1} \quad (28)$$

After each position update, particles need to recalculate their corresponding fitness value and the individuals update their individual and global best positions by evaluating the fitness of their new solution

against the fitness values of their respective individual and global best positions. This iterative process allows particles to gradually approach the optimal position within the given function range.

To address the issues of the traditional PSO algorithm in the process of particle updates, different opposition-based learning strategies are applied to individual particles in the population at different stages of iteration. The beta distribution is introduced to perturb the inertia weight ω_p . The change in the inertia weight is controlled using a random distribution, and an adjustment factor γ is introduced to make the distribution of ω_p more reasonable. This enhances particle diversity and expands the search range of the population, while also providing good local exploitation capabilities. The function formula for the beta distribution and $B(b_1, b_2)$ the update formula for the dynamic inertia weight ω_p can be expressed as:

$$B(b_1, b_2) = \int_0^1 s^{b_1-1} (1-s)^{b_2-1} ds, b_1 > 0, b_2 > 0 \quad (29)$$

$$\omega_p = \omega_{\min} + (\omega_{\min} + \omega_{\max}) \cos\left(2\pi \frac{s}{S_{\max}}\right) + \gamma B(b_1, b_2) \quad (30)$$

The gray wolf optimization algorithm, on the other hand, selects the positions of the three best individuals u , v , and w based on the ranking of the population particles. These positions, denoted as X_1 , X_2 , and X_3 , respectively, serve as guides for the iterative search process of the algorithm. Based on the principles of GWO, coefficient vectors \mathbf{A} , \mathbf{B} , and \mathbf{C} are introduced, along with the convergence factor σ and two random numbers r_3 and r_4 , uniformly distributed in the interval $[0,1]$. X_p represents the target position, and $X(s)$ denotes the position of the three best particles in the s -th generation. The iterative update of the particle positions in the population is guided by the three high ranking particles X_u , X_v , and X_w , and can be described by the following formula.

$$X_1 = X_u + A_1 B_u \quad (31)$$

$$X_2 = X_v + A_2 B_v \quad (32)$$

$$X_3 = X_w + A_3 B_w \quad (33)$$

$$X(s+1) = \frac{X_1 + X_2 + X_3}{3} \quad (34)$$

The update formulas for coefficient vectors \mathbf{A} , \mathbf{B} , and \mathbf{C} are:

$$\mathbf{A} = 2\sigma r_3 - \sigma \quad (35)$$

$$\mathbf{B} = |CX_p - X(s)| \quad (36)$$

$$\mathbf{C} = 2r_4 \quad (37)$$

The convergence factor σ controls parameter \mathbf{A} , which in turn affects the particle search range. Therefore, the beta distribution is also introduced to guide the nonlinear change of the convergence factor, so that the particle search range meets the demands of different iterations. It can improve the convergence rate of the algorithm in the early stage of iteration and the local search accuracy in the later stage. This improved convergence factor σ updating strategy can be expressed as:

$$\sigma = 2 - 2 \cos\left(\pi \frac{s}{S_{\max}}\right) - 0.1 B(b_1, b_2) \quad (38)$$

4.3. Implementation of ANN-HGPSO optimization algorithm

The implementation of the ANN-HGPSO algorithm mainly involves two modules: regression fitting and extremum-seeking optimization. The algorithm implementation process is shown in Fig. 6. The ANN regression model, which has been trained, is utilized to compute the fitness value of

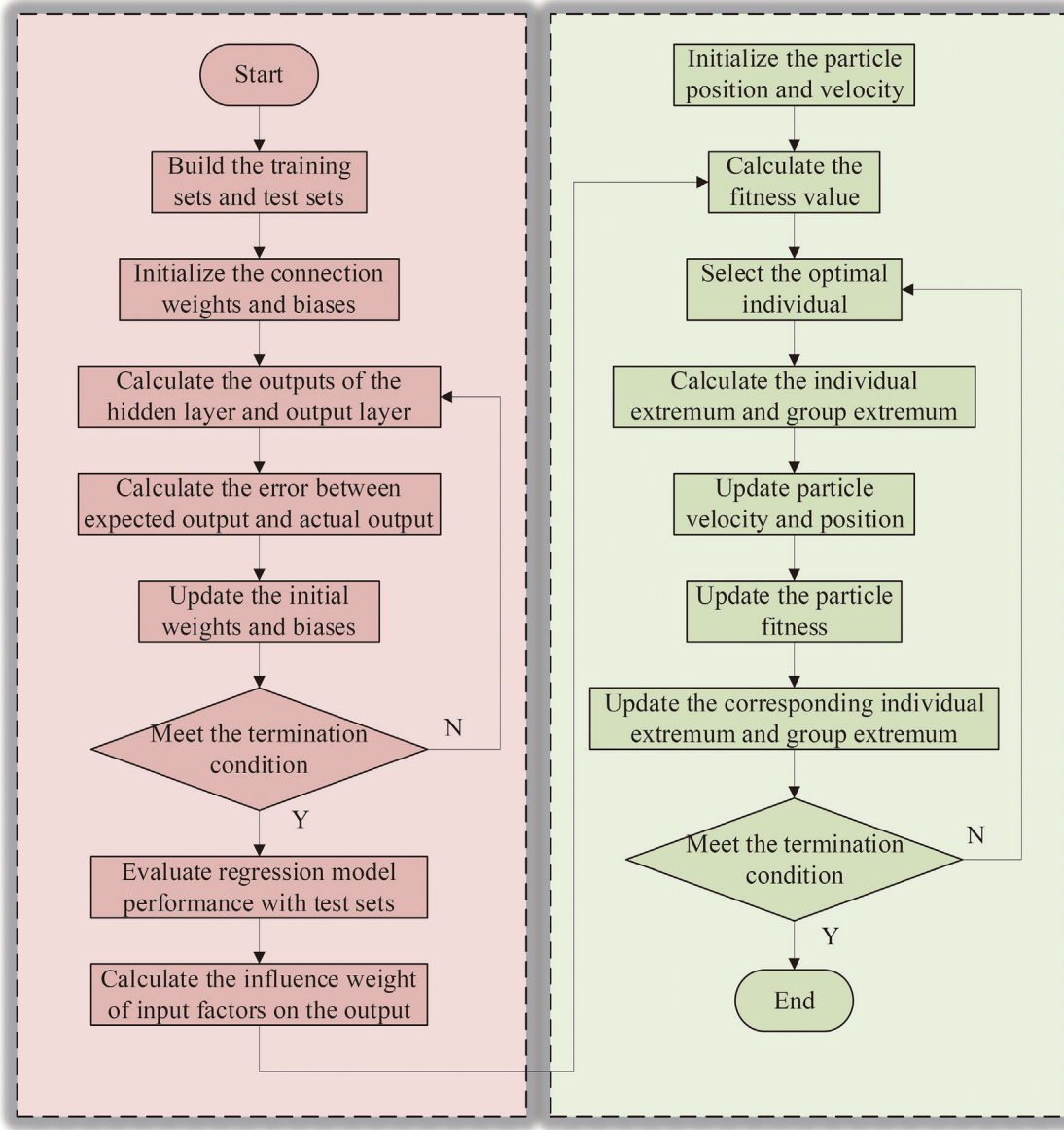


Fig. 6. Implementation process of ANN-HGPSO algorithm.

particles within the PSO algorithm. The specific implementation steps are as follows.

4.3.1. ANN regression fitting module

Step 1: Construct training and testing sets. Based on fuel cell internal resistance-operating conditions model, N sets of data samples are obtained. Choose n sets as the training set and the remaining $(N-n)$ sets as the testing set;

Step 2: Initialize the connection weights ω_{ih} between the input layer and the hidden layer, and the connection weights ω_{hj} between the hidden layer and the output layer. Also, initialize the initial biases for the hidden and output layers as m_h and n_j , respectively;

Step 3: Select the activation function and perform forward propagation to calculate the hidden layer output y_h and output layer output y_j ;

Step 4: Calculate the error between the expected output y_0 and the actual output y_j , and select the performance metric function E_{Loss} for the error function based on the gradient descent method;

Step 5: Backpropagate the error to update the connection weights ω_{ih} between the input layer and the hidden layer, the connection weights ω_{hj} between the hidden layer and the output layer, and the initial biases m_h

and n_j of the hidden and output layers, respectively. Repeat this process until the desired error is achieved;

Step 6: After feeding the test set data into the regression model, quantitatively evaluate the regression fitting performance of the model by comparing the predicted data obtained from the trained regression model with the experimental data using performance metrics such as MRE, MSE, RMSE, and R^2 ;

Step 7: By stacking the interlayer weights ω corresponding to different input factors in the regression model, the weight of the impact of distinct input factors on the output can be derived.

4.3.2. HGPSO extremum-seeking optimization module

Step 1: Initialize the population size, population dimension D , maximum number of iterations S_{max} , particle position X_k , acceleration factors c_1 and c_2 , inertia weight ω_p , and other relevant parameters;

Step 2: Compute the fitness values for the particle positions in the population, then select three best individuals u , v , and w from the population based on their fitness values. Store their corresponding particle positions in X_1 , X_2 , and X_3 respectively. Update the personal best and global best solutions based on the updated fitness values;

Step 3: Introduce the reverse learning strategy to the population particles. For the non-optimal particles, update and save their positions as $X_{\text{new}1}$;

Step 4: For the optimal particles, they follow the search iteration strategy of the grey wolf optimization algorithm, and the updated positions are saved as $X_{\text{new}2}$. $X_{\text{new}1}$ and $X_{\text{new}2}$ are merged to obtain the new particle positions X_{new} in the population;

Step 5: Update the corresponding fitness value of the particles based on their new positions, sort them and select some high-ranking particles to form a new population. Then update the individual best solution and global best solution;

Step 6: Iterate step 3 to step 5 in a loop until the termination condition is met, and obtain the optimal fitness value corresponding to the global extremum.

5. Results and discussion

5.1. Regression fitting and analysis of impact weights

Based on the internal resistance-operation conditions model, five random values within a specific range are selected as input parameters, including the operating temperature T_{stack} , anode inlet pressure P_{H_2} , cathode inlet pressure P_{air} , anode inlet humidity RH_{gas}^a and cathode inlet humidity RH_{gas}^c . Five hundred data samples are obtained under low, medium, and high current density conditions of 0.2 A/cm², 0.5 A/cm², and 1.0 A/cm², respectively. The data are divided into two parts: 350 training sets and 150 test sets, and the training and prediction processes of the ANN model are completed. The error-related evaluation parameters are listed in Table 2, and the prediction effect is shown in Fig. 7. The excellent correspondence between the forecasted data of the ANN model and the experimental data is evident, indicating a well-fitted regression of the model.

After superimposing the interlayer weights ω of different input factors corresponding to the neurons in the training model, the magnitudes of the impact weights of each input element on the output variable, the stack internal resistance R_{stack} , can be obtained under low, medium, and high current density conditions, as shown in Fig. 8. The figure intuitively reflects that under low current density environment, the order of impact weight values of five input factors is $RH_{\text{gas}}^a > P_{\text{H}_2} > T_{\text{stack}} > P_{\text{air}} > RH_{\text{gas}}^c$. Under medium current density environment, the order of impact weight values of five input factors is $RH_{\text{gas}}^a > P_{\text{H}_2} > T_{\text{stack}} > P_{\text{air}} > RH_{\text{gas}}^c$. Under high current density environment, the order of impact weight values of the five input factors is $T_{\text{stack}} > P_{\text{H}_2} > RH_{\text{gas}}^a > P_{\text{air}} > RH_{\text{gas}}^c$.

5.2. Analysis of the optimal operating condition combination

Based on the neural network training model, the range of values for the five input variables is limited according to the results in Section 3.2. The optimal operating condition combination is determined by minimizing the internal resistance R_{stack} , which indicates the optimal water management status of the PEMFC. The internal resistance is iteratively approached towards the minimum extremum within a specified range. Besides, the iterative process of the ANN-HGPSO algorithm is compared with that of the ANN-PSOGA and ANN-CPSO algorithms, and the detailed iteration process is shown in Fig. 9. From the figure, it is evident that the ANN-HGPSO algorithm used in this study is more stable compared to the traditional optimization algorithms, ANN-PSOGA and ANN-CPSO. It can rapidly approach the target extremum with fewer iterations and yields

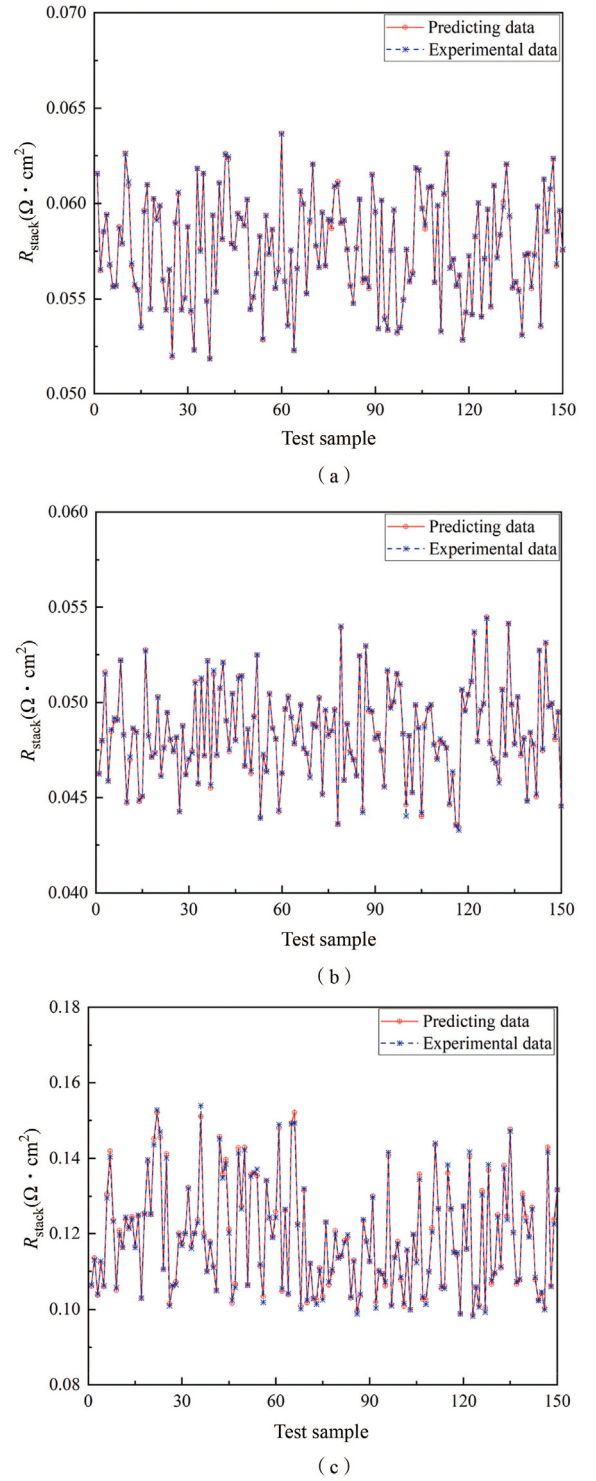


Fig. 7. Predicted results of the model. (a) 0.2 A/cm². (b) 0.5 A/cm². (c) 1.0 A/cm².

superior optimization results. The ANN-HGPSO algorithm demonstrates advantages in terms of iteration efficiency and computational accuracy. The optimal input combinations and corresponding minimum predicted values of internal resistance are obtained at low, medium, and high current densities. The humidity and actual internal resistance values are calculated for the corresponding operating condition combinations using the model described in Section 2. The numerical results are listed in Table 3.

Table 2
Predicted error parameters.

| Current density (A · cm ⁻²) | MRE (%) | MSE | RMSE | R ² |
|---|---------|------------------------|----------|----------------|
| 0.2 | 0.084 | 0.52×10^{-7} | 0.000,72 | 0.999,31 |
| 0.5 | 0.129 | 0.794×10^{-7} | 0.000,89 | 0.998,62 |
| 1.0 | 0.207 | 1.35×10^{-7} | 0.000,79 | 0.996,81 |

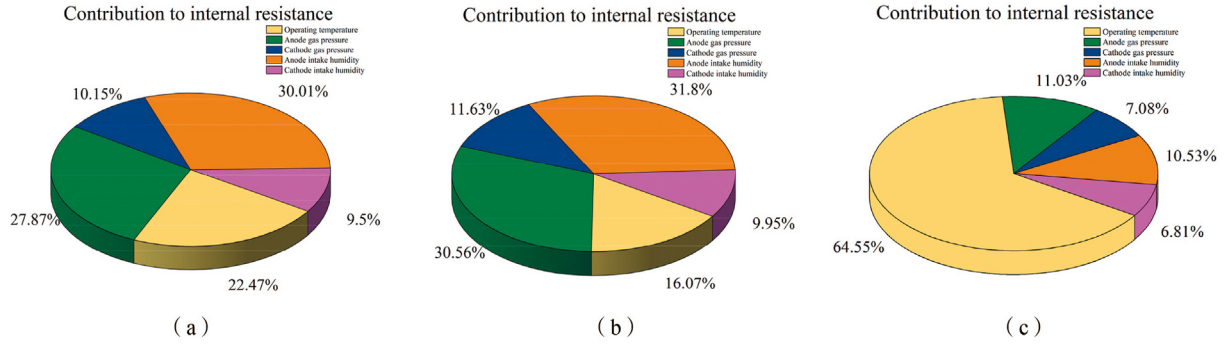


Fig. 8. Magnitude of input factor impact. (a) 0.2 A/cm². (b) 0.5 A/cm². (c) 1.0 A/cm².

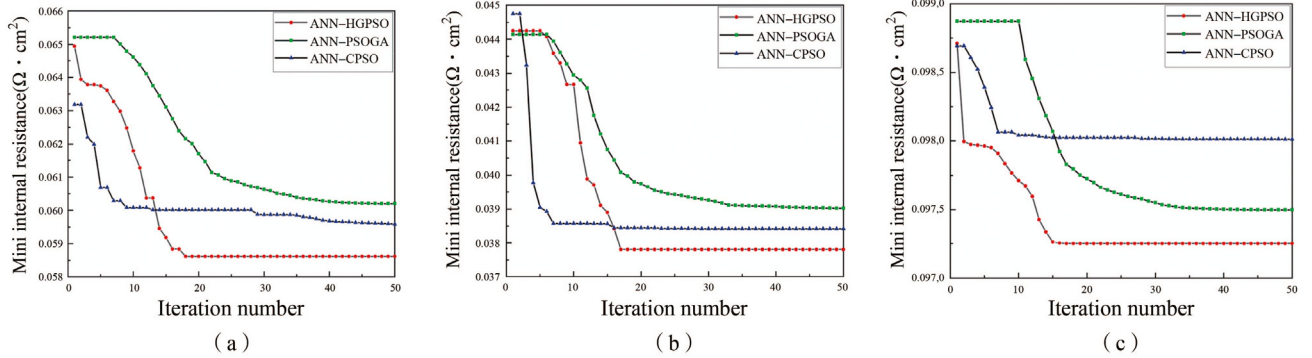


Fig. 9. Iterative process for minimum internal resistance optimization. (a) 0.2 A/cm². (b) 0.5 A/cm². (c) 1.0 A/cm².

Table 3

Optimal input combinations and corresponding extremum results.

| Factor | T (K) | P_{H_2} (bar) | P_{air} (bar) | RH_{gas}^a (%) | RH_{gas}^c (%) | R_{stack} (Ω) (Predicting) | R_{stack} (Ω) (Actual) | RH_{stack} (%) |
|--------------------|------------|--------------------|--------------------|------------------|------------------|------------------------------|--------------------------|------------------|
| Optimization (0.2) | 349.94 | 1 | 1.5 | 84.6 | 90 | 0.058,6 | 0.058,8 | 38.1 |
| Optimization (0.5) | 330 | 1 | 1.5 | 90 | 90 | 0.037,8 | 0.037 | 69.9 |
| Optimization (1.0) | 350 | 1 | 1.8 | 90 | 90 | 0.097,3 | 0.097,2 | 51.1 |

5.3. Experimental verification

The accuracy of the optimization results obtained by the algorithm can be verified using response surface methodology (RSM) experiments. RSM experiments are designed with Box-Behnken models in low, medium, and high current density conditions, and the corresponding internal resistance values are collected on the fuel cell stacks using the experimental platform shown in Fig. 10. The experimental platform primarily consists of a fuel cell testing platform (HTS-125S), the fuel cell stack, a DC electronic load (AT5800), and an impedance analyzer (Gamry Reference 3000). The fuel cell testing platform comprises a pressure supply system, a humidification system, a temperature control system, and a monitoring system. By manipulating the operating conditions such as temperature, inlet pressure, and inlet humidity using the testing platform, experimental data is collected and subjected to variance analysis. This analysis enables the derivation of regression equations and the determination of the optimized combination of operating conditions. A comparison is then made between these results and those obtained from the ANN-HGPSO algorithm to validate the feasibility and accuracy of the ANN-HGPSO method for optimization. Table 4 shows the levels of operating condition factors used for the RSM experimental design.

Based on the factors and levels in Table 4, the RSM experiment is designed using Design-Expert 12.0 software. The fuel cell testing platform utilizes a temperature control system to regulate the temperature, while the pressure control system is responsible for controlling the inlet

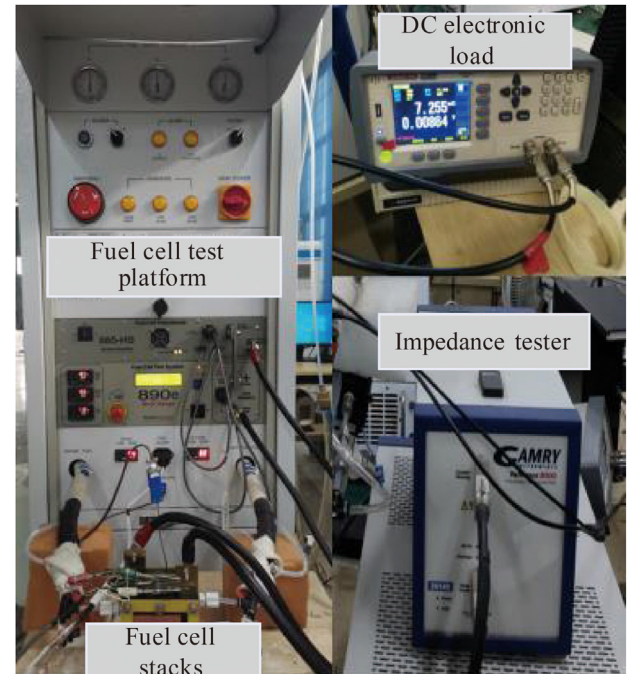


Fig. 10. Fuel cell stacks experimental platform.

Table 4

Factor levels table for RSM experimental design.

| Parameters | Factors | Levels | | |
|------------------|---------|--------|--------|---------|
| | | lowest | Medium | Highest |
| T (K) | A | 330 | 340 | 350 |
| P_{H_2} (bar) | B | 1 | 2 | 3 |
| P_{air} (bar) | C | 1.5 | 3 | 4.5 |
| RH_{gas}^a (%) | D | 30 | 60 | 90 |
| RH_{gas}^c (%) | E | 30 | 60 | 90 |

airflow to the anode and cathode to meet the desired pressure requirements. The inlet humidity is controlled by a humidifier to maintain the defined humidity level in the airflow. Additionally, flow controllers are used to maintain a constant and stable airflow of 30 L/min and 75 L/min to the anode and cathode, respectively. During the experiments, a DC electronic load is employed to control the fuel cell's operating current density at three different levels: 0.2 A/cm², 0.5 A/cm², and 1.0 A/cm². The experiments are divided into three groups based on the different current densities. In each group, the temperature, inlet pressure, and inlet humidity are adjusted according to the corresponding combinations specified in the experimental design table. The impedance testing system,

connected to a host computer, records and stores the collected internal resistance values. Furthermore, before and after each experiment group, a 10-min purge of nitrogen gas is performed to remove any excess residual water and ensure a more uniform distribution of humidity and temperature within the fuel cell. As an example, for the state of medium current density of 0.5 A/cm², different operating condition combinations and their corresponding stack internal resistance values are shown in Table 5.

The experimental data is fitted using multiple regression analysis to obtain a predictive model for the internal resistance (Y) as a function of the operating temperature (a), anode inlet pressure (b), cathode inlet pressure (c), anode inlet humidity (d), and cathode inlet humidity (e). The model can be expressed as follows:

$$R(0.5) = 0.048, 3 - 0.001, 2a + 0.002, 6b + 0.001c - 0.002, 6d - 0.000, 8e - 0.000, 8ab + 0.000, 2ac + 0.000, 3ad - 0.000, 2ae + 0.000, 1bc - 0.000, 2bd - 0.000, 1be - 0.000, 2cd + 0.000, 4ce + 0.000, 2de - 0.000, 2a^2 - 0.000, 6b^2 - 0.000, 4c^2 + 0.000, 8d^2 + 0.000, 1e^2 \quad (39)$$

Similarly, the experimental design is completed at low and high current density states, and experimental data are collected on the fuel cell stack to complete multiple regression fitting. The corresponding

Table 5

Experimental operating conditions and corresponding resistance values.

| Test number | T (K) | P_{H_2} (bar) | P_{air} (bar) | RH_{gas}^a (%) | RH_{gas}^c (%) | R_{stack} (Ω) |
|-------------|---------|-----------------|-----------------|------------------|------------------|--------------------------|
| 1 | 340 | 2 | 4.5 | 30 | 60 | 0.052,2 |
| 2 | 350 | 2 | 3 | 90 | 60 | 0.045,1 |
| 3 | 350 | 2 | 3 | 60 | 90 | 0.045,8 |
| 4 | 350 | 2 | 3 | 30 | 60 | 0.050,5 |
| 5 | 350 | 2 | 3 | 60 | 30 | 0.047,8 |
| 6 | 330 | 2 | 3 | 60 | 30 | 0.050,3 |
| 7 | 350 | 2 | 4.5 | 60 | 60 | 0.047,4 |
| 8 | 340 | 2 | 3 | 30 | 30 | 0.052,5 |
| 9 | 340 | 2 | 3 | 60 | 60 | 0.048,3 |
| 10 | 340 | 2 | 1.5 | 90 | 60 | 0.045,2 |
| 11 | 350 | 2 | 1.5 | 60 | 60 | 0.044,9 |
| 12 | 330 | 2 | 3 | 30 | 60 | 0.053,2 |
| 13 | 340 | 3 | 3 | 30 | 60 | 0.053,6 |
| 14 | 340 | 2 | 4.5 | 90 | 60 | 0.046,9 |
| 15 | 340 | 1 | 3 | 60 | 90 | 0.044,7 |
| 16 | 330 | 3 | 3 | 60 | 60 | 0.051,9 |
| 17 | 340 | 3 | 1.5 | 60 | 60 | 0.048,6 |
| 18 | 340 | 2 | 3 | 30 | 90 | 0.050,6 |
| 19 | 350 | 3 | 3 | 60 | 60 | 0.048,8 |
| 20 | 340 | 2 | 3 | 60 | 60 | 0.048,3 |
| 21 | 340 | 2 | 4.5 | 60 | 30 | 0.049,2 |
| 22 | 340 | 3 | 4.5 | 60 | 60 | 0.050,7 |
| 23 | 340 | 1 | 1.5 | 60 | 60 | 0.044,0 |
| 24 | 340 | 1 | 3 | 30 | 60 | 0.048,3 |
| 25 | 330 | 2 | 1.5 | 60 | 60 | 0.048,2 |
| 26 | 340 | 3 | 3 | 90 | 60 | 0.048,3 |
| 27 | 340 | 3 | 3 | 60 | 30 | 0.050,9 |
| 28 | 340 | 2 | 3 | 60 | 60 | 0.048,3 |
| 29 | 330 | 1 | 3 | 60 | 60 | 0.044,2 |
| 30 | 340 | 2 | 4.5 | 60 | 90 | 0.048,3 |
| 31 | 340 | 2 | 3 | 60 | 60 | 0.048,3 |
| 32 | 340 | 1 | 3 | 90 | 60 | 0.043,6 |
| 33 | 330 | 2 | 4.5 | 60 | 60 | 0.050,1 |
| 34 | 340 | 2 | 3 | 60 | 60 | 0.048,3 |
| 35 | 330 | 2 | 3 | 60 | 90 | 0.048,9 |
| 36 | 340 | 2 | 1.5 | 60 | 90 | 0.045,6 |
| 37 | 340 | 2 | 1.5 | 60 | 30 | 0.048,3 |
| 38 | 340 | 2 | 3 | 60 | 60 | 0.048,3 |
| 39 | 340 | 2 | 3 | 90 | 90 | 0.045,9 |
| 40 | 340 | 1 | 3 | 60 | 30 | 0.045,9 |
| 41 | 340 | 1 | 4.5 | 60 | 60 | 0.045,7 |
| 42 | 340 | 2 | 3 | 90 | 30 | 0.047,1 |
| 43 | 340 | 3 | 3 | 60 | 90 | 0.049,3 |
| 44 | 340 | 2 | 1.5 | 30 | 60 | 0.049,7 |
| 45 | 350 | 1 | 3 | 60 | 60 | 0.044,3 |
| 46 | 330 | 2 | 3 | 90 | 60 | 0.046,7 |

Table 6

Ranking of the impact degree of experimental factors.

| Current density | F-value | | | | | Influence degree |
|-----------------|------------|--------------------|--------------------|---------------------|---------------------|---------------------|
| | A: T (K) | B: P_{H_2} (bar) | C: P_{air} (bar) | D: RH_{gas}^a (%) | E: RH_{gas}^c (%) | |
| 0.2 | 1,052.55 | 1,522.01 | 240.5 | 2,030.07 | 177.55 | $D > B > A > C > E$ |
| 0.5 | 153.06 | 743.58 | 107.88 | 750.46 | 72.61 | $D > B > A > C > E$ |
| 1.0 | 2,351.24 | 7.9 | 0.493,3 | 3.16 | 0.222,3 | $A > B > D > C > E$ |

Table 7

Validation experiment results.

| Current density | T (K) | P_{H_2} (bar) | P_{air} (bar) | RH_{gas}^a (%) | RH_{gas}^c (%) | R_{stack} (Ω) (Predicting) | R_{stack} (Ω) (Actual) |
|-----------------|---------|-----------------|-----------------|------------------|------------------|---------------------------------------|-----------------------------------|
| 0.2 | 350 | 1 | 1.5 | 68.4 | 90 | 0.059 | 0.059,3 |
| 0.5 | 333.22 | 1 | 1.5 | 90 | 89.8 | 0.04 | 0.038,5 |
| 1.0 | 350 | 1 | 1.67 | 90 | 86.4 | 0.097 | 0.097,2 |

predictive models for the fuel cell stack impedance (Y) in each state are expressed as follows:

$$R(0.2) = 0.070,9 - 0.003,7a + 0.004,4b + 0.001,8c - 0.005,1d - 0.001,5e + 0.000,6ac - 0.000,3ad - 0.000,5ae + 0.000,7bc - 0.001,8bd - 0.000,6be - 0.001cd + 0.000,6ce + 0.000,9de + 0.000,7a^2 - 0.000,3b^2 - 0.000,7c^2 + 0.002,2d^2 + 0.000,2e^2 \quad (40)$$

$$R(1.0) = 0.115,8 - 0.026,2a - 0.001,5b - 0.000,4c + 0.001d + 0.000,3e + 0.005,3ab + 0.001,3ac - 0.003,9ad - 0.000,9ae + 0.000,3bc - 0.000,6bd - 0.000,2be - 0.000,2cd - 0.000,2ce + 0.000,1de + 0.008,6a^2 + 0.001b^2 + 0.000,1d^2 - 0.000,2e^2 \quad (41)$$

The obtained mathematical models are used to perform variance analysis on the response values Y at different current densities. The results show that the models are significant at all current densities, while the lack-of-fit terms are not significant, indicating that the models are valid and well-fitted to the actual situation. By ranking the significance parameters F of each factor through variance analysis, the influence of each factor can be obtained. The results are shown in Table 6. Comparing the results of factor influence ranking with the weight analysis results obtained by the artificial neural network algorithm, it can be found that the experimental factor influence ranking is consistent with the weight value ranking obtained by the algorithm, verifying the feasibility of obtaining influence weight through the algorithm.

According to the regression model, with the response value Y as the optimization condition, the optimal combination of operating conditions is selected within the limited range. The verification experiments are carried out on the fuel cell stacks according to the optimal operating conditions, and the corresponding actual stack resistances are collected, as shown in Table 7.

Comparing the results of the validation experiment with the optimization results obtained by the ANN-HGPSO algorithm in the previous sections, it is easy to see that under the same current density conditions, the optimal operation condition combinations obtained by the ANN-HGPSO optimization algorithm and the response surface experimental method are basically consistent, and the minimum value of the internal resistance obtained by the optimization algorithm is more excellent. Moreover, compared to the cumbersome process of the response surface experimental method, the predicted values of the extreme values obtained by the ANN-HGPSO algorithm have less differences with the actual values, and the process is more concise, which further demonstrates the efficiency and accuracy of the algorithm in optimizing the operation condition combinations to achieve the optimal water management state.

6. Conclusion

This article has established a PEMFC internal resistance-operation condition model and verified the accuracy of the model using experimental data. Based on this, the operational condition combination was optimized using the PEMFC internal resistance as the water management state indicator to achieve the optimal water management state. The following deductions can be made.

- (1) The internal resistance of the fuel cell stack exhibits a pattern of initial rapid reduction, gradual stabilization, and subsequent slow increase with the rise of current density. The activation resistance experiences a swift decline in the low current density range, while the ohmic resistance remains essentially constant across the entire current density spectrum. Meanwhile, the concentration loss resistance rises with the increase of current density in the high current density range;
- (2) Within a certain range, reducing the operating temperature, increasing the inlet humidity, and increasing the reactant gas pressure appropriately can help to reduce the internal resistance of the fuel cell and improve the output performance of the PEMFC;
- (3) The PEMFC internal resistance-operating condition model based on ANN regression fitting has high prediction accuracy. The weights of five operation conditions including operating temperature, anode and cathode inlet pressure, and anode and cathode inlet humidity obtained by the ANN-HGPSO algorithm, as well as the optimal operation conditions combination to achieve the best water management state, are verified by the response surface experimental results, which reflects the efficiency and accuracy of the ANN-HGPSO optimization algorithm.

CRediT authorship contribution

Xie Changjun: Conceptualization, Methodology. Wan Wenxin: Data curation, Software, Original draft preparation. Yang Yang: Software, Investigation. Li Yang: Supervision. Song Jie: Literature review. Deng Zhanfeng: Validation. Tan Jinting: Experimental design. Zhang Ruiming: Data collection.

Declaration of competing interest

The authors declare that they have no known competing financial interests or personal relationships that could have appeared to influence the work reported in this paper.

Acknowledgements

This work was supported by the National Key Research and Development Project of China (2020YFB1506802); and the Key Research and Development Project of Guangdong Province (2020B0909040004).

References

- [1] Yang B, Li JL, Li YL, Guo ZX, Zeng KD, Shu HC. A critical survey of proton exchange membrane fuel cell system control: summaries, advances, and perspectives. *Int J Hydrogen Energy* 2022;47(17):9986–10020.
- [2] Lu XQ, Qu Y, Wang YD, Qin C, Liu G. A comprehensive review on hybrid power system for PEMFC-HEV: issues and strategies. *Energy Convers Manag* 2018;171:1273–91.
- [3] Liu XW, Yang Y, Zhang LX, Zhou SP, Xu LM, Xie CJ, et al. Uncertainty assessment of a semi-empirical output voltage model for proton exchange membrane fuel cells. *Int J Hydrogen Energy* 2023;48(29):11071–85.
- [4] Li HW, Xu BS, Lu GL, Du CH, Huang N. Multi-objective optimization of PEM fuel cell by coupled significant variables recognition, surrogate models and a multi-objective genetic algorithm. *Energy Convers Manag* 2021;236:114063.
- [5] Giner-Sanz JJ, Ortega EM, Pérez-Herranz V. Mechanistic equivalent circuit modelling of a commercial polymer electrolyte membrane fuel cell. *J Power Sources* 2018;379:328–37.
- [6] Zhang YY, Huang C, Huang HL, Wu JD. Multiple learning neural network algorithm for parameter estimation of proton exchange membrane fuel cell models. *Green Energy and Intelligent Transportation* 2023;2(1):100040.
- [7] Nalbant Y, Colpan CO, Devrim Y. Development of a one-dimensional and semi-empirical model for a high temperature proton exchange membrane fuel cell. *Int J Hydrogen Energy* 2018;43:5939–50.
- [8] Jahnke T, Futter G, Latz A, Malkow T, Papakonstantinou G, Tsotridis G. Performance and degradation of proton exchange membrane fuel cells: state of the art in modeling from atomistic to system scale. *J Power Sources* 2016;304:207–33.
- [9] Daniele V, Andrea C, Andrea B. Validation of a pseudo 2D analytical model for high temperature PEM fuel cell impedance valid at typical operative conditions. *Electrochim Acta* 2019;310:122–35.
- [10] Kahveci EE, Taymaz I. Assessment of single-serpentine PEM fuel cell model developed by computational fluid dynamics. *Fuel* 2018;217:51–8.
- [11] Giner-Sanz JJ, Ortega EM, Pérez-Herranz V. Statistical analysis of the effect of temperature and inlet humidities on the parameters of a semiempirical model of the internal resistance of a polymer electrolyte membrane fuel cell. *J Power Sources* 2018;381:84–93.
- [12] Khan SS, Shareef H, Ibrahim AA. Improved semi-empirical model of proton exchange membrane fuel cell incorporating fault diagnostic feature. *J of Modern Power Sys and Clean Energy* 2021;9:1566–73.
- [13] Tiss F, Chouikh R, Guizani A. Dynamic modeling of a PEM fuel cell with temperature effects. *Int J Hydrogen Energy* 2013;38:8532–41.
- [14] Niya MR, Hoorfar M. Process modeling of the ohmic loss in proton exchange membrane fuel cells. *Electrochim Acta* 2014;120:193–203.
- [15] Niya MR, Phillips RK, Hoorfar M. Process modeling of the impedance characteristics of proton exchange membrane fuel cells. *Electrochim Acta* 2016;191:594–605.
- [16] Dai W, Wang HJ, Yuan XZ, Martin JJ, Yang DJ, Qiao JL. A review on water balance in the membrane electrode assembly of proton exchange membrane fuel cells. *Int J Hydrogen Energy* 2009;34:9461–78.
- [17] Wang ZQ, Zeng YC, Sun SC, Shao ZG, Yi BL. Improvement of PEMFC water management by employing water transport plate as bipolar plate. *Int J Hydrogen Energy* 2017;42(34):21922–9.
- [18] Futter GA, Gazdzicki P, Friedrich KA, Latz A, Jahnke T. Physical modeling of polymer-electrolyte membrane fuel cells: understanding water management and impedance spectra. *J Power Sources* 2018;391:148–61.
- [19] Kim JY, Luo G, Wang CY. Modeling liquid water redistributions in biporous layer flow-fields of proton exchange membrane fuel cells. *J Power Sources* 2018;400:284–95.
- [20] Salahuddin M, Uddin MN, Hwang G, Asmatulu R. Superhydrophobic PAN nanofibers for gas diffusion layers of proton exchange membrane fuel cells for cathodic water management. *Int J Hydrogen Energy* 2018;43:11530–8.
- [21] Hernandez-Gomez A, Ramirez V, Guilbert D, Saldivar B. Cell voltage static-dynamic modeling of a PEM electrolyzer based on adaptive parameters: development and experimental validation. *Renew Energy* 2021;163:1508–22.
- [22] Zhang JL, Tang YH, Song CJ, Xia ZT, Li H, Wang HJ. PEM fuel cell relative humidity (RH) and its effect on performance at high temperatures. *Electrochim Acta* 2008;53(16):5315–21.
- [23] Lin R, Diao XY, Ma TC, Tang SH, Chen L, Liu DC. Optimized microporous layer for improving polymer exchange membrane fuel cell performance using orthogonal test design. *Appl Energy* 2019;254:113714.
- [24] Xia S, Lin R, Cui X, Shan J. The application of orthogonal test method in the parameters optimization of PEMFC under steady working condition. *Int J Hydrogen Energy* 2016;41:11380–90.
- [25] Wang B, Lin R, Liu D, Xu J, Feng B. Investigation of the effect of humidity at both electrode on the performance of PEMFC using orthogonal test method. *Int J Hydrogen Energy* 2019;44:13737–43.
- [26] Kanani H, Shams M, Hasheminasab M, Bozorgnezhad A. Model development and optimization of operating conditions to maximize PEMFC performance by response surface methodology. *Energy Convers Manag* 2015;93:9–22.
- [27] Mocotéguy P, Ludwig B, Steiner NY. Application of current steps and design of experiments methodology to the detection of water management faults in a proton exchange membrane fuel cell stack. *J Power Sources* 2016;303:126–36.
- [28] Boeta NR, Martinez CO, Kunusch C. On the anode pressure and humidity regulation in PEM fuel cells: a nonlinear predictive control approach. *IFAC-PapersOnLine* 2015;48(23):434–9.
- [29] Yan XQ, Hou M, Sun LY, Liang D, Shen Q, Xu HF. AC impedance characteristics of a 2kW PEM fuel cell stack under different operating conditions and load changes. *Int J Hydrogen Energy* 2007;32(17):4358–64.
- [30] Pandiyan S, Jayakumar K, Rajalakshmi N, Dhathathreyan KS. Thermal and electrical energy management in a PEMFC stack – an analytical approach. *Int J Heat Mass Tran* 2008;51(3):469–73.
- [31] Chen X, Xu JH, Fang Y, Li WB, Ding YJ, Wan ZM. Temperature and humidity management of PEM fuel cell power system using multi-input and multi-output fuzzy method. *Appl Therm Eng* 2022;203:117865.
- [32] Peng XB, Wu WQ, Zhang YK, Yang W. Determination of operating parameters for PEM fuel cell using support vector machines approach. *J Energy Storage* 2017;13:409–17.
- [33] Yang Y, Zhu WC, Li Y, Zhao B, Xie CJ. Modeling of PEMFC and analysis of multiple influencing factors on output characteristics. *J Electrochem Soc* 2022;3:169.
- [34] Nanadegani FS, Lay EN, Iranzo A, Salva JA, Sundén B. On neural network modeling to maximize the power output of PEMFCs. *Electrochim Acta* 2020;348:136345.
- [35] Chugh S, Chaudhari C, Sonkar K, Sharma A, Kapur GS, Ramakumar SSV. Experimental and modelling studies of low temperature PEMFC performance. *Int J Hydrogen Energy* 2020;45(15):8866–74.
- [36] Jiao K, Li XG. Water transport in polymer electrolyte membrane fuel cells. *Prog Energy Combust Sci* 2011;37(3):221–91.
- [37] Rubio MA, Urquía A, Dormido S. Diagnosis of PEM fuel cells through current interruption. *J Power Sources* 2007;171(2):670–7.
- [38] Cano-Andrade S, Hernandez-Guerrero A, Spakovsky MR, Damian-Ascencio CE, Rubio-Arana JC. Current density and polarization curves for radial flow field patterns applied to PEMFCs (Proton Exchange Membrane Fuel Cells). *Energy* 2010;35(2):920–7.
- [39] Kan V, Sangswang A, Naetiladdanon S, Mujjalinvimut E. PEM fuel cell emulator based on dynamic model with relative humidity calculation. In: 2017 14th International Conference on Electrical Engineering/ Electronics, Computer, Telecommunications and Information Technology (ECTI-CON); 2017.
- [40] Chen X, Xu JH, Liu Q, Chen Y, Wang XD, Li WB, et al. Active disturbance rejection control strategy applied to cathode humidity control in PEMFC system. *Energy Convers Manag* 2020;224:113389.
- [41] Laribi S, Mammari K, Sahli Y, Koussa K. Air supply temperature impact on the PEMFC impedance. *J Energy Storage* 2018;17:327–35.
- [42] Tang Y, Zhang J, Song C. Temperature dependent performance and in situ AC impedance of high-temperature PEM fuel cells using the nafion-112 membrane. *J Electrochem Soc* 2006;11:2036–43.
- [43] Sun Z, Cao D, Ling Y, Xiang F, Sun Z, Wu F. Proton exchange membrane fuel cell model parameter identification based on dynamic differential evolution with collective guidance factor algorithm. *Energy* 2021;216:119056.